Title: Evaluation of 4D Flow MRI-based non-invasive pressure assessment in aortic coarctations

Authors: Simone Saitta[1,2], Selene Pirola[2], Filippo Piatti[3], Emiliano Votta[1], Federico Lucherini[1], Francesca Pluchinotta[4], Mario Carminati[4], Massimo Lombardi[5], Christian Geppert[6], Federica Cuomo[7], Carlos Alberto Figueroa[7], Xiao Yun Xu[2], Alberto Redaelli[1]

Affiliations:

[1]*Department of Electronics Information and Bioengineering, Politecnico di Milano, Milan, Italy*

[2]*Department of Chemical Engineering, Imperial College London, London, UK*

[3]*3D and Computer Simulation Laboratory, IRCCS Policlinico San Donato, San Donato Milanese, Italy*

[4]*Department of Paediatric Cardiology and Adult Congenital Heart Disease, IRCCS Policlinico San Donato, San Donato Milanese, Italy*

[5]*Multimodality Cardiac Imaging Section, IRCCS Policlinico San Donato, San Donato Milanese, Milan, Italy*

[6]*Siemens Healthcare GmbH, Erlangen, Germany*

[7]*Departments of Surgery and Biomedical Engineering, University of Michigan, MI, USA*

Corresponding author: Alberto Redaelli

Address: Via Ponzio 35/5, 20133 Milano, Italy

Telephone: +39-02-23993360

Fax: +39-02-23993360

Email: alberto.redaelli@polimi.it

Word count (Introduction through Discussion): 3509

Abstract

Severity of aortic coarctation (CoA) is currently assessed by estimating trans-coarctation pressure drops through cardiac catheterization or echocardiography. In principle, more detailed information could be obtained non-invasively based on space- and time-resolved magnetic resonance imaging (4D flow) data. Yet the limitations of this imaging technique require testing the accuracy of 4D flow-derived hemodynamic quantities against other methodologies.

With the objective of assessing the feasibility and accuracy of this non-invasive method to support the clinical diagnosis of CoA, we developed an algorithm (4DF-FEPPE) to obtain relative pressure distributions from 4D flow data by solving the Poisson pressure equation. 4DF-FEPPE was tested against results from a patient-specific fluid-structure interaction (FSI) simulation, whose patient-specific boundary conditions were prescribed based on 4D flow data. Since numerical simulations provide noise-free pressure fields on fine spatial and temporal scales, our analysis allowed to assess the uncertainties related to 4D flow noise and limited resolution.

4DF-FEPPE and FSI results were compared on a series of cross-sections along the aorta. Bland-Altman analysis revealed very good agreement between the two methodologies in terms of instantaneous data at peak systole, end-diastole and time-averaged values: biases (means of differences) were +0.4 mmHg, -1.1 mmHg and +0.6 mmHg, respectively. Limits of agreement (2 SD) were ±0.978 mmHg, ±1.06 mmHg and ±1.97 mmHg, respectively. Peak-to-peak and maximum trans-coarctation pressure drops obtained with 4DF-FEPPE differed from FSI results by 0.75 mmHg and -1.34 mmHg respectively. The present study considers important validation aspects of non-invasive pressure difference estimation based on 4D flow MRI, showing the potential of this technology to be more broadly applied to the clinical practice.

Keywords: Aortic coarctation, 4D flow MRI, Pressure Poisson equation, Non-invasive pressure difference estimation, Fluid dynamics.

1. Introduction

In aortic coarctation (CoA), the narrowed aortic lumen represents an abnormal impedance to flow which increases the afterload on the left ventricle, resulting in high blood pressure in the upper part of the body and often ventricular hypertrophy, degenerative alterations in the proximal aorta and systemic hypertension (LaDisa et al., 2011; Lantz et al., 2013). CoA severity is assessed based on the trans-coarctation pressure difference: the American College of Cardiology guidelines (Warnes et al., 2008) recommend intervention for CoA repair if the peak-to-peak coarctation pressure difference measured by cardiac catheterization exceeds 20 mmHg. Despite being considered a clinical gold standard, catheterization is an invasive procedure and European ESC guidelines recommend the non-invasive evaluation of CoA severity using imaging techniques (Baumgartner et al., 2010). Among these, the most commonly used is Doppler echocardiography, which enables to estimate pressure drops using the simplified Bernoulli equation (Donati et al., 2017). More recently, 4D phase-contrast magnetic resonance imaging (4D PC-MRI or 4D flow) was proposed as an alternative to catheterization and Doppler. 4D flow allows for measurement of *in vivo* blood flow, providing three-directional velocity fields in a volume of interest throughout the cardiac cycle (Markl et al., 2016). An increasing number of studies have assessed the reliability of various 4D flow-derived hemodynamic markers that could support the diagnosis and prognosis of cardiovascular diseases and the timing of intervention (Ha et al., 2016, 2017; Piatti et al., 2017). For instance, flow distribution quantification has been shown to yield predictive information on cerebral ischemia (Bagan et al., 2006), and vortices assessment in pulmonary arteries has been applied to pulmonary hypertension diagnosis (Reiter et al., 2014). Intravascular pressure fields can be derived from 4D flow-based velocity fields through numerical methods that yield the approximate solution of the Navier-Stokes equations. Among the main proposed numerical formulations (Bertoglio et al., 2018), the solution of the pressure Poisson equation (PPE) has shown robustness and ease of implementation (Krittian et al., 2012). Nonetheless, 4D flow measurements are affected by noise-like phase errors arising

from tissue motion, and are limited by low spatial and temporal resolutions and partial volume effects, which hamper the quantification of parameters, including pressure drops, that require computing velocity space- or time-derivatives (Ha et al., 2016; Ong et al., 2015). These sources of uncertainty question the reliability of such estimations in the real clinical setting and make it necessary to validate 4D flow-derived results against pressures obtained through other well-controlled methodologies. Bock et al. (2011) used *in vitro* experiments on stenosis phantoms to compare MR-derived pressure drops with the established Doppler-based method. *In vitro* phantoms provide highly reproducible experimental conditions, but the Bernoulli formula often leads to pressure drop overestimation (Itu et al., 2013) and Doppler ultrasound is operator-dependent; hence, it represents a suboptimal term of comparison. Important work was conducted by Riesenkampff et al. (2014) and Goubergrits et al. (2019) who compared *in vivo* trans-coarctation pressure drops computed from 4D flow data by solving the PPE vs. direct cardiac catheterization measurements, obtaining an overall good agreement. However, in Riesenkampff et al. (2014) spatial uncertainties in pressure catheter locations or biases related to catheter-induced flow alterations were present but not investigated. In Goubergrits et al. (2019), potential errors due to catheter location were accounted for. Additionally, the authors provided new important evidence of how limited 4D flow spatial resolution affects pressure mapping. Still, catheter measurements can only give pressure values at predefined locations along the aorta, hence preventing an exhaustive validation of the whole distribution of 4D flow-based pressure drop data.

In order to overcome the aforementioned limitations, in the present study we compared the relative pressure distribution obtained from 4D flow data acquired *in vivo* on a CoA patient to the highly space- and time-resolved results of the corresponding patient-specific fluid-structure interaction (FSI) model. This approach allowed to evaluate the accuracy of the method in terms of pressure distributions over time, since for every 4D flow-derived datum an FSI datum at the same location was available. Moreover,

and in contrast with invasive measurements, pressures obtained through FSI were not affected by flow disturbances potentially introduced by catheters.

Hence, the aim of this study was to assess the feasibility and accuracy of a non-invasive method based on a finite element solution of the PPE (FE-PPE), through a comprehensive validation against a detailed computational model, in the specific context of CoA.

2. Methods

2.1. Mathematical and Numerical Formulations

For a given velocity field, the corresponding pressure field (p) can be derived from the Navier-Stokes equation, whose weak form can be obtained following the procedure described in (Krittian et al., 2012); find $p \in H^1(\Omega)$ such that:

$$\int_\Omega \nabla p \cdot \nabla q \, d\Omega = \int_\Omega \vec{b} \cdot \nabla q \, d\Omega, \quad \forall q \in H^1(\Omega). \tag{1}$$

Where q is a test function and Ω is the computational domain. The term $\vec{b}$ is defined as:

$$\vec{b} = -\rho\left(\frac{\partial \vec{v}}{\partial t} + \vec{v} \cdot \nabla \vec{v} - g\right) + \mu \Delta \vec{v}, \tag{2}$$

where $\vec{v}$ is velocity, ρ is density, g describes a distribution of external forces, and μ is dynamic viscosity.

Adopting a standard Galerkin finite element approximation, equation (1) can be expressed as a linear system (Meier et al., 2010):

$$\mathrm{K}p = \sum_{l=1,2,3} \mathrm{L}^{x_l} b^{x_l}, \tag{3}$$

where K is the stiffness matrix and L^{x_l} is a non-symmetric matrix defined as:

$$\mathrm{L}_{i,j}^{x_l} := \int_\Omega N_i \frac{\partial N_j}{\partial x_l}, \qquad l = 1,2,3 \tag{4}$$

where N_i are the finite element shape functions (Meier et al., 2010). In contrast with (Krittian et al., 2012), linear, instead of tricubic, Lagrangian shape functions were used to limit computational expense. Velocity

derivatives in equation (2) were calculated using finite difference schemes and the numerical framework for the solution of the PPE was implemented in MATLAB (Mathworks, Natick, MA, USA). For a unique solution of p a reference pressure must be defined at a certain (arbitrary) point: in the present study p=0 was imposed at the most distal point of the aorta for all time steps; therefore all pressure results obtained from the algorithm (referred to as 4DF-FEPPE) are pressure differences with respect to this reference point.

2.2. Workflow

4D flow MRI data acquired for a CoA patient were used to calculate pressures through the numerical framework of 4DF-FEPPE and to prescribe boundary conditions for the FSI simulation (Figure 1). Upon testing velocity field yielded by the FSI simulation vs. the raw 4D flow data, pressure data obtained through 4DF-FEPPE were evaluated against FSI pressure results.

2.3. Data Acquisition and Geometry Reconstruction

4D flow MRI and contrast-enhanced magnetic resonance angiographic (MRA) acquisitions for a 57-year-old male patient with CoA were provided by the Multimodality Cardiac Imaging Section, IRCCS Policlinico San Donato (San Donato Milanese, Milan, Italy). Using a Magnetom Aera 1.5T scanner (Siemens Healthcare, Erlangen, Germany), *VENC* values were set to 150 cm/s for all directions and 21 time frames were obtained over the cardiac cycle. Maximum velocity magnitude was observed to be equal to 253 cm/s. 4D flow isotropic in-plane resolution and slice thickness were set to 2.08 mm and 2.4 mm, respectively. Temporal resolution was equal to 40 ms and echo time to 2.4 ms. MRA isotropic in-plane resolution and slice thickness were set to 1.56 mm and 1.60 mm, respectively.

Using in-house MATLAB code, velocity fields were converted from the corresponding phase-contrast images and 4D flow datasets were corrected for aliasing. The gold standard manual segmentation was performed by an expert operator to extract the patient's 3D geometry. Segmentation was carried out in

itkSNAP from the MRA images using the brush tool. The segmented volume was exported as a *.stl* file and smoothed in Meshmixer (Autodesk, San Rafaeil, CA, USA) using the software embedded shape-preserving smoothing filter. In the smoothed model, coarctation cross-sectional area was equal to 0.84 cm^2, while aortic inlet and outlet cross-sections were 10.6 cm^2 and 2.5 cm^2 wide, respectively. This volume (shown in red in Figure 2a) was used for the FSI simulation (Figure 2b). The same *.stl* model was registered onto the 4D flow volume and used as computational domain for 4DF-FEPPE. For this purpose, to avoid the errors due to 4D flow measurements near the vessel boundaries, boundary voxels were excluded from the 4DF-FEPPE computational domain by an inward extrusion of the *.stl* model equal to the voxel size. This operation was done using Meshmixer 'Extrude' filter followed by the shape-preserving smoothing filter.

2.4. Patient-Specific FSI Simulation

The patient's aortic geometry, previously segmented in itkSNAP from the MRA images (Figure 2a), was imported in CRIMSON (Figueroa et al., 2006; *www.crimson.software*) and discretized into a mesh consisting of~4M tetrahedral elements using the software embedded meshing tools. Maximum element size was set to 0.9 mm and an exponential growth ratio between adjacent layers close to the boundary was chosen, with a minimum element size of 0.2 mm and a total thickness of 2 mm. Flow rate through a cross-section in the ascending aorta was extracted from 4D flow data and imposed at the model inlet using a parabolic velocity profile. A three-element Windkessel model (3E-WKM) was coupled to each outlet, i.e., brachiocephalic trunk (BCT), left carotid artery (LCA), left subclavian artery (LSA) and descending aorta (DAo), to account for the downstream hydraulic impedances (Figure 2b). 3E-WKM parameters (Table 1) were calculated following the procedure described in (Pirola et al., 2017). Mean flow rate values for each outlet were obtained from 4D flow data analysis, while mean pressures were assumed equal to 80 mmHg for all outlets. Two consecutive cardiac cycles were simulated. A 5% or less change in maximum velocity magnitude and outlet pressures was considered for assuming periodicity and the

second cycle was used for result analysis. Maximum convergence residuals and time step were set to 10^{-5} and 0.002 s, respectively. Blood was modelled as a Newtonian fluid with viscosity μ=4 cP and density ρ=1060 kg/m^3. The aortic wall was assumed 1 mm thick (Kim et al., 2009) and with a homogeneous, elastic and isotropic stress-strain behaviour (Young modulus E=878 kPa, Poisson ratio ν=0.5). According to Moens-Korteweg equation (Cavalcante et al., 2011), these parameters correspond to a pulse wave velocity of approximately 5.25 m/s, which is in agreement with previous studies on CoA stiffness (Xu et al., 1997) and with the value used to tune the 3E-WKM parameters. Computations were performed on 24 cores (Intel® Xeon® CPU E5-2640 v3 2.60 GHz).

Table 1. *Windkessel parameter values used in the numerical simulation: proximal resistance (R_p), compliance (C) and distal resistance (R_d) for the brachiocephalic trunk (BCT), left carotid artery (LCA), left subclavian artery (LSA) and descending aorta (DAo).*

Outlet	R_p [g·mm^{-4}·s^{-1}]	C [mm^4·s^2·g^{-1}]	R_d [g·mm^{-4}·s^{-1}]
BCT	0.0294	12.1872	0.1281
LCA	0.0872	1.2950	1.3955
LSA	0.0418	3.7653	0.4682
DAo	0.0203	10.0218	0.1583

3. Results

3.1. Quantification of Results

To quantify the agreement between FSI results and 4D flow raw data, outlet flow rates over time and velocity color maps were analyzed. Correlation coefficients were calculated to quantify similarity between flow rate curves. Relative root-mean-square errors (RRMSE) and 2D correlation coefficients (2DCC) were calculated between velocity maps determined by 4D flow and FSI to provide an average quantification of

their consistency. Then, to better assess spatial differences in velocity profiles, normalized grayscale differences (NGD) were obtained for three cross-sections along the aorta.

To evaluate the agreement between 4DF-FEPPE and FSI pressure results throughout the aortic domain, a Bland-Altman analysis was performed by taking into account a series of cross-sections along the aorta. Finally, as most clinically relevant measures, trans-coarctation pressure drops calculated with 4DF-FEPPE were compared to corresponding FSI data.

3.2. FSI Model Verification vs. 4D Flow Raw Data

Overall, a good match was found between time-dependent outlet flow rates obtained with FSI and 4D flow data (Figure 3): the largest difference in time-averaged flow rate was 0.26 L/min (+20.6%) at the LSA. In the LSA and in the BCT flow rate waveform were fully consistent with 4D flow data, whereas in the DAo the FSI simulation results showed an underestimation of the peak flow rate by 1.43 L/min (-18.25%) and a slower temporal decay, possibly due to an underestimation of the patient's true aortic wall stiffness. Correlation coefficients between the flow rate curves were equal to 0.9746, 0.8786, 0.9846 and 0.9403 for the BCT, LCA, LSA and DAo, respectively.

Space distribution of velocity magnitude in the descending aorta on one sagittal (Figure 4a) and three cross-sectional planes (P1, P2 and P3; Figure 4b, c) was compared at several time-points during systole (T1, …, T9). The high velocity jet created by the coarctation narrowing could be observed clearly at the longitudinal plane (Figure 4a), but the flow jet in the simulation results lasted longer in time, covered a larger volume of the descending aorta and showed a sharper high-velocity propagation front (time points T6 and T8), which might be due to the Newtonian fluid modelling assumption. RRMSE (Sarrami-Foroushani et al., 2015) and 2DCC (Table 2) confirmed the good agreement between simulation and 4D flow, with values ranging from 0.168 to 0.364 and from 0.628 to 0.911 respectively. On P1 (Figure 4c), FSI results showed a peak velocity region near the left side wall, in agreement with 4D flow data; at T5 and T9, the FSI simulation captured secondary flow features that were not observed in 4D flow measurements.

Additionally, the high velocity profile obtained from the simulation appeared more flattened against the wall: phenomenon which could be better appreciated at T3 in the NGD images (Figure 4c). Similarly, on P2, complex secondary flows and more irregular high velocity profiles were resolved by the finer FSI grid, while they seemed to be averaged out by 4D flow lower resolution; differences in high velocity regions could possibly be due to small discrepancies in coarctation orifice shape. On P3, at T5 4D velocity contours showed a high velocity region that was not observed in the simulation results due to the aforementioned peak flow rate underestimation through the DAo. At T9, good agreement was found in terms of velocity profile.

Table 2. *Normalized root mean square errors (RMSE) and 2D correlation coefficients (CC) between FSI and 4D flow velocity magnitude contours on the selected planes for the specified time points.*

		Time-Points					
		T3		**T5**		**T9**	
		RMSE	**2DCC**	**RMSE**	**2DCC**	**RMSE**	**2DCC**
Cross-sectional Planes	**P1**	0.168	0.886	0.239	0.847	0.213	0.833
	P2	0.220	0.681	0.364	0.628	0.319	0.638
	P3	0.222	0.911	0.333	0.883	0.252	0.829

3.3. Comparison between 4DF-FEPPE and FSI Pressure Fields

On 19 different cross-sections along the aorta (Figure 5a), plane-averaged values of the pressure difference with respect to the DAo outlet were compared through a Bland-Altman analysis. Instantaneous values at peak systole and at end diastole, as well as time-averaged values, obtained with the two approaches were considered (Figure 5b, c, d). Biases (means of differences) were +0.4, +1.1 and +0.6 mmHg for peak systolic, end-diastolic and time-averaged values, respectively. The corresponding limits of agreement (2 standard deviation of differences) were ±0.978 mmHg, ±1.97 mmHg and ±1.06 mmHg,

respectively. For peak systole and time average pressures almost all data points lie in the 95% limit band, which shows good agreement between the two methodologies along the whole aorta.

Trans-coarctation pressure difference curves over time obtained with 4DF-FEPPE were consistent with simulation results (Figure 6a) throughout the cardiac cycle. Peak-to-peak (Δp_{pp}) and maximum (Δp_m) pressure drops between two cross-sectional planes located immediately proximally and distally to the coarctation were compared between the two approaches (Figure 6b, Table 3). Δp_{pp} corresponds to the difference between pressure peaks over time, Δp_m is the maximum instantaneous pressure difference over time.

Table 3. *Maximum and peak-to-peak pressure drops (in mmHg) obtained from the FSI simulation and 4DF-FEPPE.*

	Δp_m	Δp_{pp}
FSI	22.43	16.85
4DF-FEPPE	21.09	17.6

Pressure difference contours were compared at three different time points in the cardiac cycle are reported in Figure 6c, where simulation results are shown as pressure differences relative to the DAo. Both 4D flow-derived pressure and FSI simulation results showed pressure distributions typically observed in CoA patients, with a clear difference between regions proximal and distal to the narrowing.

4. Discussion

The present study represents an evaluation of pressure mapping from 4D flow MRI using a numerical framework for the FE-PPE referred to as 4DF-FEPPE. Our methodology was applied to a specific case of CoA, where pressure assessment is of diagnostic importance. Relatively low *VENC* values of the 4D flow acquisition were set pursuing an optimal trade-off between the need for capturing high velocity jets in the coarctation region and improving the signal-to-noise ratio in 4D flow measurements at lower velocity

241 regions, including the post-coarctation region. Minor aliasing effects were associated to this setting and
242 were filtered out.
243 Given the limitations of 4D flow, and the uncertainties related to this technology, which must be carefully
244 addressed before its clinical application, we assessed the feasibility of our non-invasive pressure
245 estimation method by comparison with the pressures obtained with a specifically designed FSI simulation.
246 Unlike 4D flow, FSI simulations provide noise-free velocity and pressure fields on arbitrarily fine spatial
247 and temporal scales. Therefore, our analysis allowed to investigate the uncertainties related to 4D flow
248 noise and limited spatial and temporal resolutions.
249 Our approach differs from Riesenkampff et al. (2014) and Goubergrits et al. (2019) one, where the
250 reliability of MR-derived trans-coarctation pressure drops was investigated by a comparison with catheter
251 measurements. In both studies, the authors performed a Bland-Altman analysis on a cohort of patients,
252 whereas only one patient was included in our work. However, the nature of our comparison allowed to
253 perform a similar analysis by comparing pressures at different locations within the aorta. Riesenkampff et
254 al. reported limits of agreement of ±9.6 mmHg and ±9.7 mmHg for peak-systolic and end-diastolic
255 pressure differences respectively, around ten times greater than the ones obtained in our study (±0.978
256 and ±1.97 mmHg, respectively). Considering peak-to-peak trans-coarctation differences (Δp_{pp}),
257 Riesenkampff et al. (2014) found good agreement between 4D flow-based and direct measurements, with
258 discrepancies ranging from 0 to 5 mmHg, while Goubergrits et al. (2019) reported differences between 0
259 and 6.5 mmHg. In our study, a discrepancy in Δp_{pp} of 0.75 mmHg was obtained.
260 Goubergrits et al. (2019), Riesenkampff et al. (2014) and Bock et al. (2011) all mentioned the tendency of
261 the MR-based method to underestimate pressure with respect to catheters or echocardiography
262 respectively. Bock et al. (2011) reported MR-based peak pressure differences that underestimated
263 echocardiography by 60.1 ± 17.8%. Nevertheless, the authors themselves argued that echocardiography
264 could have overestimated pressure differences. In our comparison with FSI results we did not observe this

bias, further suggesting an overestimation of Doppler-based methods and, possibly, of catheter measurements as well (De Vecchi et al., 2014; Olesen et al., 2018). On the contrary, in our Bland-Altman analysis 4D flow-based results had biases (mean of differences) of +0.4 mmHg and -1.1 mmHg at peak-systole and end-diastole, respectively, consistently with the -0.6 mmHg and -0.3 mmHg values found by Riesenkampff et al. (2014).

The validity of our approach relied on the accuracy of the FSI model, which was supported by the good consistency between the flow field computed by FSI modelling and the raw 4D flow velocity data.

The flow rates for the three supra-aortic branches and DAo obtained *in silico* were in agreement with 4D flow, with errors between time-averaged values of 3.94%, 11.6%, 20.6% and 0.838% for the BCT, LCA, LSA and DAo respectively. In a recent validation study of CFD results with 4D flow, Biglino et al. (2015) reported similar errors in mean flow rates, equal to 3.53%, 1.69%, 4.35% and 14.2%, respectively.

A potential limitation of our FSI model consisted in having imposed a non-patient-specific velocity profile, which might also affect pressure drop results (Goubergrits et al., 2013). Nonetheless, recent studies (Madhavan and Kemmerling, 2018; Pirola et al., 2018) have shown how, albeit modelling 3D inlet velocity profiles is important for evaluating hemodynamics in the ascending aorta, differences in flow solutions are negligible beyond two diameters distal to the inlet. For the patient analysed in the present study, the distance along the centreline from the inlet to the site of the coarctation was found equal to 16.8 cm; enough for the velocity profile to develop, given the inlet diameter of 3.7 cm. The comparison between velocity color maps along the descending aorta further confirmed the accuracy of the FSI model, which also captured late systolic secondary flow features that were not detected by 4D flow owing to its lower spatial resolution. Also, RMSE between velocity magnitude color maps ranged from 16% to 36%; despite the higher complexity of our fluid domain, these results are in agreement with a previous study focused on the CFD *vs.* 4D flow comparison in a carotid artery (Sarrami-Foroushani et al., 2015), which reported RRMSE values ranging from 10% to 20%.

No information about the patient's pressure at any location was available and a mean value of 80 mmHg was used to set 3E-WKM parameters for all outlets. Albeit this was an inevitable modeling limitation, the good agreement between FSI flow fields and 4D flow data confirmed the goodness of this assumption. Finally, the worse matching of flow rate curves in the DAo could be due to an underestimation of the true ascending aorta stiffness. A higher aortic compliance could have resulted in increased energy stored proximal to the coarctation, leading to higher diastolic flow rate through the post-coarctation region (DeGroff et al., 2003). Although it is in principle possible to estimate patient-specific vessel wall mechanical properties from PC-MRI (Ou et al., 2008), a variety of methodologies have been proposed (Wentland et al., 2014) and recent evidence suggests that different methods can give significantly different results (Dyverfeldt et al., 2014). Given this uncertainty in estimating mechanical properties from MRI, we used parameters taken from recent literature. Despite many researchers developed constitutive models for the healthy aortic wall (Prendergast et al., 2003), there is great scarcity of studies reporting parameters for vascular tissue in unrepaired CoA. The Young's modulus and thickness values used in the present study were taken from (Kim et al. 2009), where they were obtained for an untreated case of CoA with similar geometry. The chosen mechanical properties yielded a good match between FSI results and raw 4D flow data in terms of flow distributions and velocity magnitude contours.

Calculating pressure from 4D flow using 4DF-FEPPE took approximately 4 minutes for a 21-frame dataset. Future work will focus on 4D flow MRI pre-processing, including advanced noise reduction and clever spatiotemporal upsampling techniques to improve extraction of *in vivo* hemodynamic features. Current efforts are aimed at the application of the developed method on a larger patient cohort, in order to test its robustness as a non-invasive diagnostic tool.

Acknowledgements

Simone Saitta was supported by the scholarship “Tesi all’estero” a.a. 2017/2018 –first bid, issued by Politecino di Milano with D.Dirn. 5772 prot.n. 88510 of 29/09/2017. Selene Pirola was supported by the European Commission within the Horizon 2020 Framework through the MSCA-ITN-ETN (642458).

Conflict of interest statement

The authors declare that there is no conflict of interest regarding the content of this article.

Appendix A – Mesh Sensitivity Analysis

A mesh sensitivity analysis was performed by running steady flow simulations in CRIMSON using meshes consisting of ∼1.4, ∼2.4 and ∼4 million tetrahedral elements. A steady flow rate corresponding to systolic peak was imposed at the inlet, while zero pressure was set for all outlets. Similar velocity patterns were captured by all three meshes, but different maximum values of velocity magnitude within the narrowing were computed with the different grids. To choose the best suited mesh, the maximum velocity magnitude value on a cross-section within the coarctation was chosen as parameter of grid convergence. Then, the Grid Convergence Index (GCI) (Roache, 1998) was calculated for the fine-to-medium and medium-to-coarse grid refinements as described in (Craven et al., 2009). The *GCI* is a measure of how much the variable of interest (trans-coarctation maximum velocity magnitude) is different from the asymptotic numerical value; it indicates how much the calculated variable of interest would change with a further grid refinement (Craven et al., 2009; Sakri et al., 2016). Let the subscripts 1, 2, 3 indicate the fine, medium and coarse meshes respectively:

$$r \approx \left(\frac{N_1}{N_2}\right)^{1/3} \approx \left(\frac{N_2}{N_3}\right)^{1/3}, \tag{A1}$$

$$p = \frac{\log\left(\frac{f_3 - f_2}{f_2 - f_1}\right)}{\log r}, \tag{A2}$$

$$E_1 = \frac{\frac{f_2 - f_1}{f_1}}{r^p - 1}, \; E_2 = \frac{\frac{f_3 - f_2}{f_2}}{r^p - 1}, \tag{A3, A4}$$

$$GCI_{1,2} = F_s \cdot |E_1|, \quad GCI_{2,3} = F_s \cdot |E_2|, \tag{A5, A6}$$

where N is the number of elements, f is the parameter of interest and F_s is the "factor of safety" equal to 1.25 (Craven et al., 2009). In particular, f_1 = 1:871 m/s, f_2 = 1:849 m/s and f_3 = 1:8209 m/s were found. The mesh sensitivity analysis revealed that the solution computed by the fine was relatively insensitive to further mesh refinement, and the grid chosen herein was the fine one, corresponding to a grid $GCI_{1,2}$ of approximately 3.4%, which is in agreement with *GCI*s reported in recent studies (Craven et al., 2009; Tedaldi et al., 2018). Additionally, to ensure that grids were in the asymptotic range of convergence the ratio:

$$k = \frac{GCI_{2,3}}{r^p \cdot GCI_{1,2}}, \tag{A7}$$

was calculated, and the relation $k \approx 1$ was satisfied.

References

Bagan, P., Vidal, R., Martinod, E., Destable, M.-D., Tremblay, B., Dumas, J.L., Azorin, J.F., 2006. Cerebral Ischemia during Carotid Artery Cross-Clamping: Predictive Value of Phase-Contrast Magnetic Resonance Imaging. Ann. Vasc. Surg. 20, 747–752. https://doi.org/10.1007/s10016-006-9126-8

Baumgartner, H., Bonhoeffer, P., De Groot, N.M.S., de Haan, F., Deanfield, J.E., Galie, N., Gatzoulis, M.A., Gohlke-Baerwolf, C., Kaemmerer, H., Kilner, P., Meijboom, F., Mulder, B.J.M., Oechslin, E., Oliver, J.M., Serraf, A., Szatmari, A., Thaulow, E., Vouhe, P.R., Walma, E., ESC Committee for Practice Guidelines (CPG), Vahanian, A., Auricchio, A., Bax, J., Ceconi, C., Dean, V., Filippatos, G., Funck-Brentano, C., Hobbs, R., Kearney, P., McDonagh, T., Popescu, B.A., Reiner, Z., Sechtem, U., Sirnes, P.A., Tendera, M., Vardas,

P., Widimsky, P., Document Reviewers, McDonagh, T., Swan, L., Andreotti, F., Beghetti, M., Borggrefe, M., Bozio, A., Brecker, S., Budts, W., Hess, J., Hirsch, R., Jondeau, G., Kokkonen, J., Kozelj, M., Kucukoglu, S., Laan, M., Lionis, C., Metreveli, I., Moons, P., Pieper, P.G., Pilossoff, V., Popelova, J., Price, S., Roos-Hesselink, J., Uva, M.S., Tornos, P., Trindade, P.T., Ukkonen, H., Walker, H., Webb, G.D., Westby, J., 2010. ESC Guidelines for the management of grown-up congenital heart disease (new version 2010): The Task Force on the Management of Grown-up Congenital Heart Disease of the European Society of Cardiology (ESC). Eur. Heart J. 31, 2915–2957. https://doi.org/10.1093/eurheartj/ehq249

Bertoglio, C., Nuñez, R., Galarce, F., Nordsletten, D., Osses, A., 2018. Relative pressure estimation from velocity measurements in blood flows: State-of-the-art and new approaches. Int. J. Numer. Methods Biomed. Eng. 34, e2925. https://doi.org/10.1002/cnm.2925

Biglino, G., Cosentino, D., Steeden, J.A., De Nova, L., Castelli, M., Ntsinjana, H., Pennati, G., Taylor, A.M., Schievano, S., 2015. Using 4D Cardiovascular Magnetic Resonance Imaging to Validate Computational Fluid Dynamics: A Case Study. Front. Pediatr. 3. https://doi.org/10.3389/fped.2015.00107

Bock, J., Frydrychowicz, A., Lorenz, R., Hirtler, D., Barker, A.J., Johnson, K.M., Arnold, R., Burkhardt, H., Hennig, J., Markl, M., 2011. In vivo noninvasive 4D pressure difference mapping in the human aorta: phantom comparison and application in healthy volunteers and patients. Magn. Reson. Med. 66, 1079–1088. https://doi.org/10.1002/mrm.22907

376 Cavalcante, J.L., Lima, J.A.C., Redheuil, A., Al-Mallah, M.H., 2011. Aortic stiffness: current
377 understanding and future directions. J. Am. Coll. Cardiol. 57, 1511–1522.
378 https://doi.org/10.1016/j.jacc.2010.12.017
379 Craven, B.A., Paterson, E.G., Settles, G.S., Lawson, M.J., 2009. Development and Verification of
380 a High-Fidelity Computational Fluid Dynamics Model of Canine Nasal Airflow. J.
381 Biomech. Eng. 131, 091002-091002–11. https://doi.org/10.1115/1.3148202
382 De Vecchi, A., Clough, R.E., Gaddum, N.R., Rutten, M.C.M., Lamata, P., Schaeffter, T.,
383 Nordsletten, D.A., Smith, N.P., 2014. Catheter-Induced Errors in Pressure Measurements
384 in Vessels: An In-Vitro and Numerical Study. IEEE Trans. Biomed. Eng. 61, 1844–1850.
385 https://doi.org/10.1109/TBME.2014.2308594
386 DeGroff, C.G., Orlando, W., Shandas, R., 2003. Insights into the effect of aortic compliance on
387 Doppler diastolic flow patterns seen in coarctation of the aorta: a numeric study. J. Am.
388 Soc. Echocardiogr. Off. Publ. Am. Soc. Echocardiogr. 16, 162–169.
389 https://doi.org/10.1067/mje.2003.20
390 Donati, F., Myerson, S., Bissell, M.M., Smith, N.P., Neubauer, S., Monaghan, M.J., Nordsletten,
391 D.A., Lamata, P., 2017. Beyond Bernoulli. Circ. Cardiovasc. Imaging 10, e005207.
392 https://doi.org/10.1161/CIRCIMAGING.116.005207
393 Dyverfeldt, P., Ebbers, T., Länne, T., 2014. Pulse wave velocity with 4D flow MRI: Systematic
394 differences and age-related regional vascular stiffness. Magn. Reson. Imaging 32, 1266–
395 1271. https://doi.org/10.1016/j.mri.2014.08.021

Ebbers, T., Wigström, L., Bolger, A.F., Engvall, J., Karlsson, M., 2001. Estimation of relative cardiovascular pressures using time-resolved three-dimensional phase contrast MRI. Magn. Reson. Med. 45, 872–879.

Figueroa, C.A., Vignon-Clementel, I.E., Jansen, K.E., Hughes, T.J.R., Taylor, C.A., 2006. A coupled momentum method for modeling blood flow in three-dimensional deformable arteries. Comput. Methods Appl. Mech. Eng., John H. Argyris Memorial Issue. Part II 195, 5685–5706. https://doi.org/10.1016/j.cma.2005.11.011

Goubergrits, L., Hellmeier, F., Neumann, D., Mihalef, V., Gulsun, M.A., Chinali, M., Secinaro, A., Runte, K., Schubert, S., Berger, F., Kuehne, T., Hennemuth, A., Kelm, M., 2019. Patient-specific requirements and clinical validation of MRI-based pressure mapping: A two-center study in patients with aortic coarctation. J. Magn. Reson. Imaging JMRI 49, 81–89. https://doi.org/10.1002/jmri.26230

Goubergrits, L., Mevert, R., Yevtushenko, P., Schaller, J., Kertzscher, U., Meier, S., Schubert, S., Riesenkampff, E., Kuehne, T., 2013. The impact of MRI-based inflow for the hemodynamic evaluation of aortic coarctation. Ann. Biomed. Eng. 41, 2575–2587. https://doi.org/10.1007/s10439-013-0879-2

Ha, H., Kim, G.B., Kweon, J., Lee, S.J., Kim, Y.-H., Lee, D.H., Yang, D.H., Kim, N., 2016. Hemodynamic Measurement Using Four-Dimensional Phase-Contrast MRI: Quantification of Hemodynamic Parameters and Clinical Applications. Korean J. Radiol. 17, 445–462. https://doi.org/10.3348/kjr.2016.17.4.445

Ha, H., Lantz, J., Ziegler, M., Casas, B., Karlsson, M., Dyverfeldt, P., Ebbers, T., 2017. Estimating the irreversible pressure drop across a stenosis by quantifying turbulence production using 4D Flow MRI. Sci. Rep. 7, 46618. https://doi.org/10.1038/srep46618

http://www.crimson.software/, n.d.

Itu, L., Sharma, P., Ralovich, K., Mihalef, V., Ionasec, R., Everett, A., Ringel, R., Kamen, A., Comaniciu, D., 2013. Non-invasive hemodynamic assessment of aortic coarctation: validation with in vivo measurements. Ann. Biomed. Eng. 41, 669–681. https://doi.org/10.1007/s10439-012-0715-0

Kim, H.J., Vignon-Clementel, I.E., Figueroa, C.A., LaDisa, J.F., Jansen, K.E., Feinstein, J.A., Taylor, C.A., 2009. On Coupling a Lumped Parameter Heart Model and a Three-Dimensional Finite Element Aorta Model. Ann. Biomed. Eng. 37, 2153–2169. https://doi.org/10.1007/s10439-009-9760-8

Krittian, S.B.S., Lamata, P., Michler, C., Nordsletten, D.A., Bock, J., Bradley, C.P., Pitcher, A., Kilner, P.J., Markl, M., Smith, N.P., 2012. A finite-element approach to the direct computation of relative cardiovascular pressure from time-resolved MR velocity data. Med. Image Anal. 16, 1029–1037. https://doi.org/10.1016/j.media.2012.04.003

LaDisa, J.F., Alberto Figueroa, C., Vignon-Clementel, I.E., Jin Kim, H., Xiao, N., Ellwein, L.M., Chan, F.P., Feinstein, J.A., Taylor, C.A., 2011. Computational Simulations for Aortic Coarctation: Representative Results From a Sampling of Patients. J. Biomech. Eng. 133, 91008-NaN. https://doi.org/10.1115/1.4004996

436 Lantz, J., Ebbers, T., Engvall, J., Karlsson, M., 2013. Numerical and experimental assessment of
437 turbulent kinetic energy in an aortic coarctation. J. Biomech. 46, 1851–1858.
438 https://doi.org/10.1016/j.jbiomech.2013.04.028
439 Madhavan, S., Kemmerling, E.M.C., 2018. The effect of inlet and outlet boundary conditions in
440 image-based CFD modeling of aortic flow. Biomed. Eng. OnLine 17.
441 https://doi.org/10.1186/s12938-018-0497-1
442 Markl, M., Schnell, S., Wu, C., Bollache, E., Jarvis, K., Barker, A.J., Robinson, J.D., Rigsby, C.K.,
443 2016. Advanced flow MRI: emerging techniques and applications. Clin. Radiol. 71, 779–
444 795. https://doi.org/10.1016/j.crad.2016.01.011
445 Meier, S., Hennemuth, A., Friman, O., Bock, J., Markl, M., Preusser, T., 2010. Non-invasive 4D
446 blood flow and pressure quantification in central blood vessels via PC-MRI, in: 2010
447 Computing in Cardiology. Presented at the 2010 Computing in Cardiology, pp. 903–906.
448 Olesen, J.B., Villagómez-Hoyos, C.A., Møller, N.D., Ewertsen, C., Hansen, K.L., Nielsen, M.B.,
449 Bech, B., Lönn, L., Traberg, M.S., Jensen, J.A., 2018. Noninvasive Estimation of Pressure
450 Changes Using 2-D Vector Velocity Ultrasound: An Experimental Study WithIn
451 VivoExamples. IEEE Trans. Ultrason. Ferroelectr. Freq. Control 65, 709–719.
452 https://doi.org/10.1109/TUFFC.2018.2808328
453 Ong, F., Uecker, M., Tariq, U., Hsiao, A., Alley, M.T., Vasanawala, S.S., Lustig, M., 2015. Robust
454 4D flow denoising using divergence-free wavelet transform. Magn. Reson. Med. 73,
455 828–842. https://doi.org/10.1002/mrm.25176
456 Ou, P., Celermajer, D.S., Mousseaux, E., Giron, A., Aggoun, Y., Szezepanski, I., Sidi, D., Bonnet,
457 D., 2007. Vascular remodeling after “successful” repair of coarctation: impact of aortic

458 arch geometry. J. Am. Coll. Cardiol. 49, 883–890.
459 https://doi.org/10.1016/j.jacc.2006.10.057
460 Ou, P., Celermajer, D.S., Raisky, O., Jolivet, O., Buyens, F., Herment, A., Sidi, D., Bonnet, D.,
461 Mousseaux, E., 2008. Angular (Gothic) aortic arch leads to enhanced systolic wave
462 reflection, central aortic stiffness, and increased left ventricular mass late after aortic
463 coarctation repair: evaluation with magnetic resonance flow mapping. J. Thorac.
464 Cardiovasc. Surg. 135, 62–68. https://doi.org/10.1016/j.jtcvs.2007.03.059
465 Piatti, F., Pirola, S., Bissell, M., Nesteruk, I., Sturla, F., Della Corte, A., Redaelli, A., Votta, E.,
466 2017. Towards the improved quantification of in vivo abnormal wall shear stresses in
467 BAV-affected patients from 4D-flow imaging: Benchmarking and application to real data.
468 J. Biomech. 50, 93–101. https://doi.org/10.1016/j.jbiomech.2016.11.044
469 Pirola, S., Cheng, Z., Jarral, O.A., O'Regan, D.P., Pepper, J.R., Athanasiou, T., Xu, X.Y., 2017. On
470 the choice of outlet boundary conditions for patient-specific analysis of aortic flow using
471 computational fluid dynamics. J. Biomech. 60, 15–21.
472 https://doi.org/10.1016/j.jbiomech.2017.06.005
473 Pirola, S., Jarral, O.A., O'Regan, D.P., Asimakopoulos, G., Anderson, J.R., Pepper, J.R.,
474 Athanasiou, T., Xu, X.Y., 2018. Computational study of aortic hemodynamics for patients
475 with an abnormal aortic valve: The importance of secondary flow at the ascending aorta
476 inlet. APL Bioeng. 2, 026101. https://doi.org/10.1063/1.5011960
477 Prendergast, P.J., Lally, C., Daly, S., Reid, A.J., Lee, T.C., Quinn, D., Dolan, F., 2003. Analysis of
478 Prolapse in Cardiovascular Stents: A Constitutive Equation for Vascular Tissue and Finite-
479 Element Modelling. J. Biomech. Eng. 125, 692–699. https://doi.org/10.1115/1.1613674

Reiter, G., Reiter, U., Kovacs, G., Olschewski, H., Fuchsjäger, M., 2014. Blood Flow Vortices along the Main Pulmonary Artery Measured with MR Imaging for Diagnosis of Pulmonary Hypertension. Radiology 275, 71–79. https://doi.org/10.1148/radiol.14140849

Riesenkampff, E., Fernandes, J.F., Meier, S., Goubergrits, L., Kropf, S., Schubert, S., Berger, F., Hennemuth, A., Kuehne, T., 2014. Pressure Fields by Flow-Sensitive, 4D, Velocity-Encoded CMR in Patients With Aortic Coarctation. JACC Cardiovasc. Imaging 7, 920. https://doi.org/10.1016/j.jcmg.2014.03.017

Roache, P.J., 1998. Verification and validation in computational science and engineering. Hermosa, Albuquerque, NM.

Sakri, F.M., Ali, M.S.M., Salim, S.A.Z.S., 2016. Computational investigations and grid refinement study of 3D transient flow in a cylindrical tank using OpenFOAM. IOP Conf. Ser. Mater. Sci. Eng. 152, 012058. https://doi.org/10.1088/1757-899X/152/1/012058

Sarrami-Foroushani, A., Nasr Esfahany, M., Nasiraei Moghaddam, A., Saligheh Rad, H., Firouznia, K., Shakiba, M., Ghanaati, H., Wilkinson, I.D., Frangi, A.F., 2015. Velocity Measurement in Carotid Artery: Quantitative Comparison of Time-Resolved 3D Phase-Contrast MRI and Image-based Computational Fluid Dynamics. Iran. J. Radiol. Q. J. Publ. Iran. Radiol. Soc. 12, e18286. https://doi.org/10.5812/iranjradiol.18286

Tedaldi, E., Montanari, C., Aycock, K.I., Sturla, F., Redaelli, A., Manning, K.B., 2018. An experimental and computational study of the inferior vena cava hemodynamics under respiratory-induced collapse of the infrarenal IVC. Med. Eng. Phys. 54, 44–55. https://doi.org/10.1016/j.medengphy.2018.02.003

Warnes, C.A., Williams, R.G., Bashore, T.M., Child, J.S., Connolly, H.M., Dearani, J.A., Del Nido, P., Fasules, J.W., Graham, T.P., Hijazi, Z.M., Hunt, S.A., King, M.E., Landzberg, M.J., Miner, P.D., Radford, M.J., Walsh, E.P., Webb, G.D., 2008. ACC/AHA 2008 Guidelines for the Management of Adults with Congenital Heart Disease: Executive Summary: a report of the American College of Cardiology/American Heart Association Task Force on Practice Guidelines (writing committee to develop guidelines for the management of adults with congenital heart disease). Circulation 118, 2395–2451. https://doi.org/10.1161/CIRCULATIONAHA.108.190811

Wentland, A.L., Grist, T.M., Wieben, O., 2014. Review of MRI-based measurements of pulse wave velocity: a biomarker of arterial stiffness. Cardiovasc. Diagn. Ther. 4, 193–206. https://doi.org/10.3978/j.issn.2223-3652.2014.03.04

Xu, J., Shiota, T., Omoto, R., Zhou, X., Kyo, S., Ishii, M., Rice, M.J., Sahn, D.J., 1997. Intravascular ultrasound assessment of regional aortic wall stiffness, distensibility, and compliance in patients with coarctation of the aorta. Am. Heart J. 134, 93–98. https://doi.org/10.1016/S0002-8703(97)70111-X

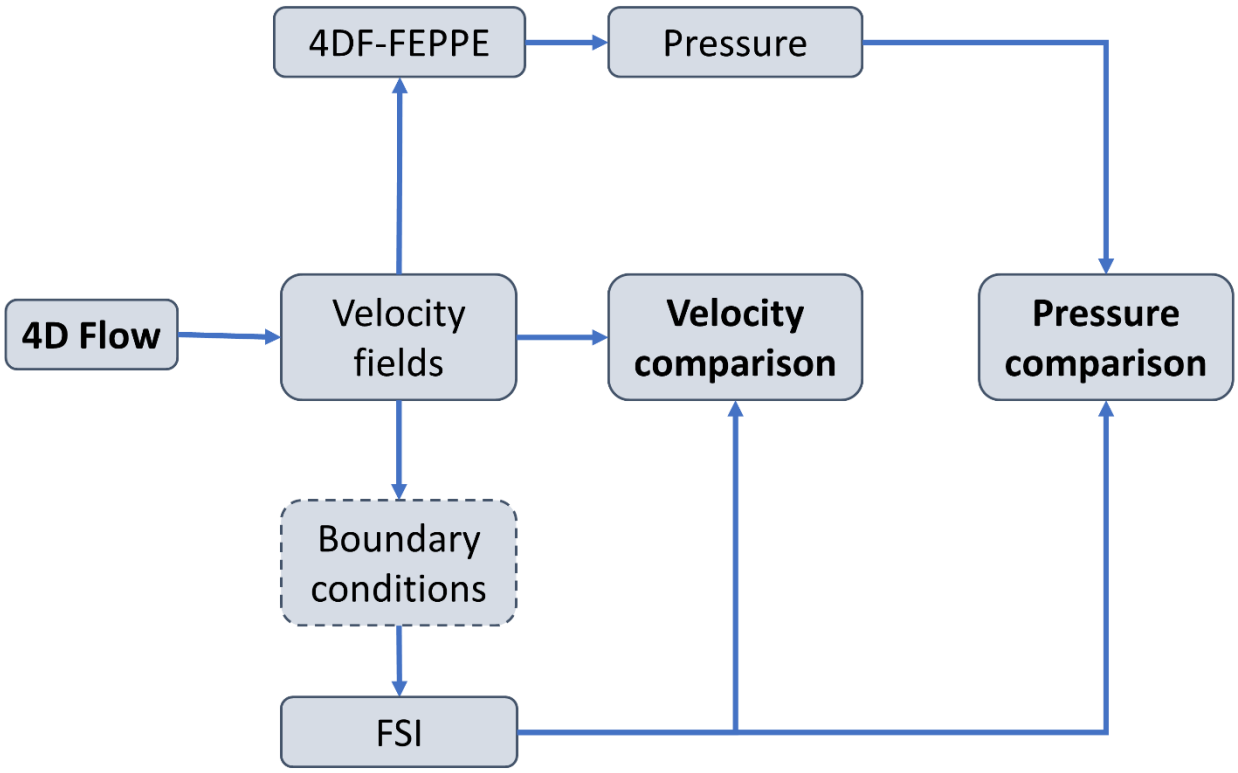

517

518 **Figure 1.** Schematic representation of the adopted workflow. 4D flow MRI data were used as input to 4DF-FEPPE

519 and as boundary conditions for the FSI simulation. FSI simulation results were first compared with raw 4D flow data

520 in terms of flow fields and then compared with 4DF-FEPPE pressure results.

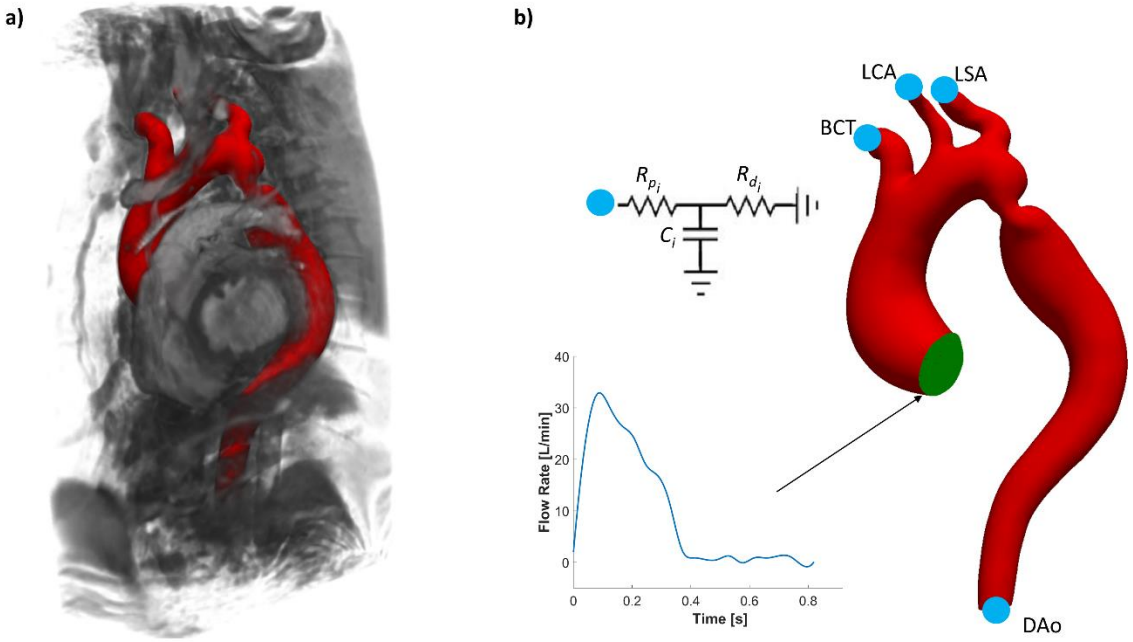

Figure 2. (a) Segmented 3D geometry (red) superimposed on a volumetric representation of MRA images. (b) FSI simulation setup with patient-specific time-dependent flow rate curve imposed at the inlet (in green) and 3E-WKM at the outlets. Different parameters were set for each outlet.

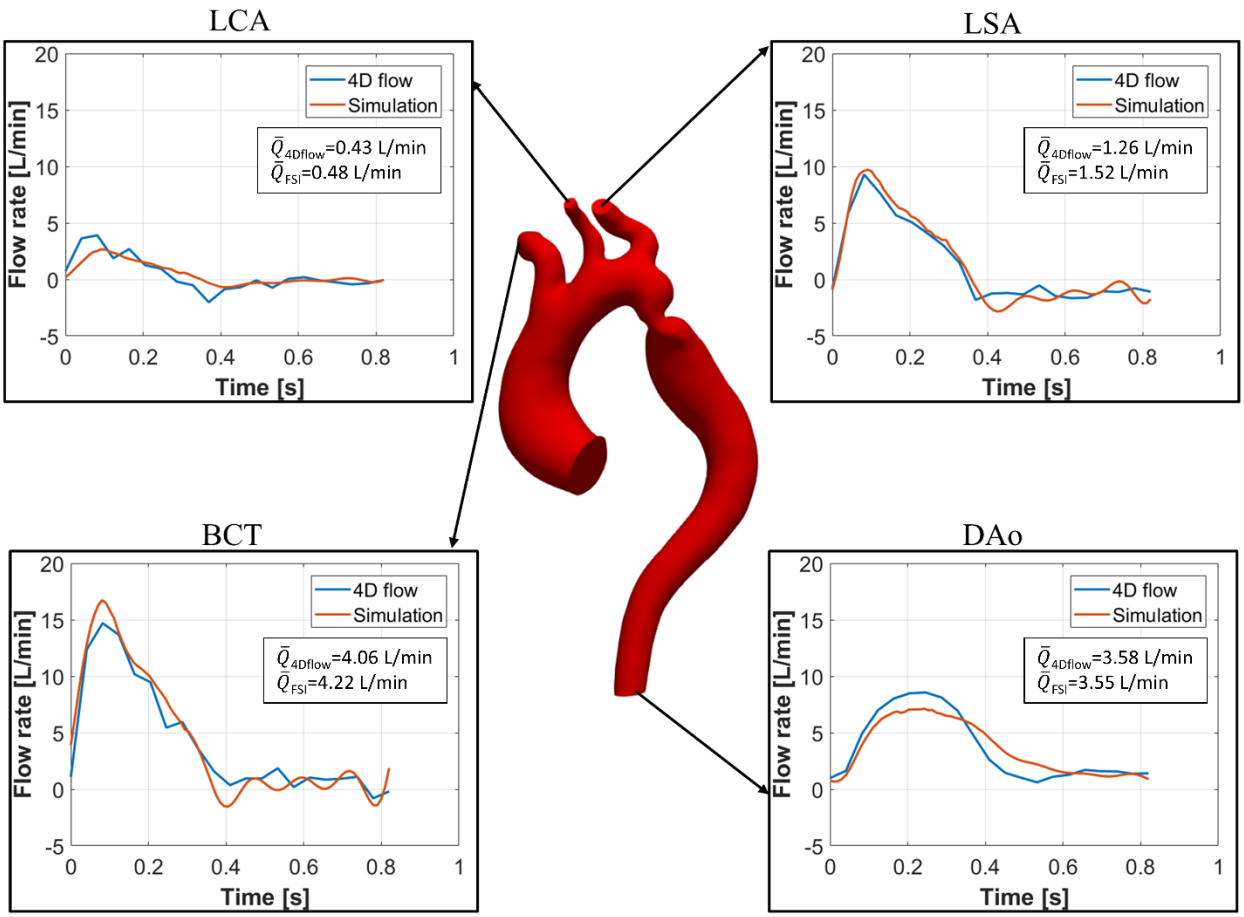

Figure 3. Outlet flow rates over time from FSI simulation results (red lines) compared to 4D flow data (blue lines). $\bar{Q}$=time-averaged flow rate. LCA=left carotid artery; LSA= left subclavian artery; BCT=brachiocephalic trunk; DAo= descending aorta.

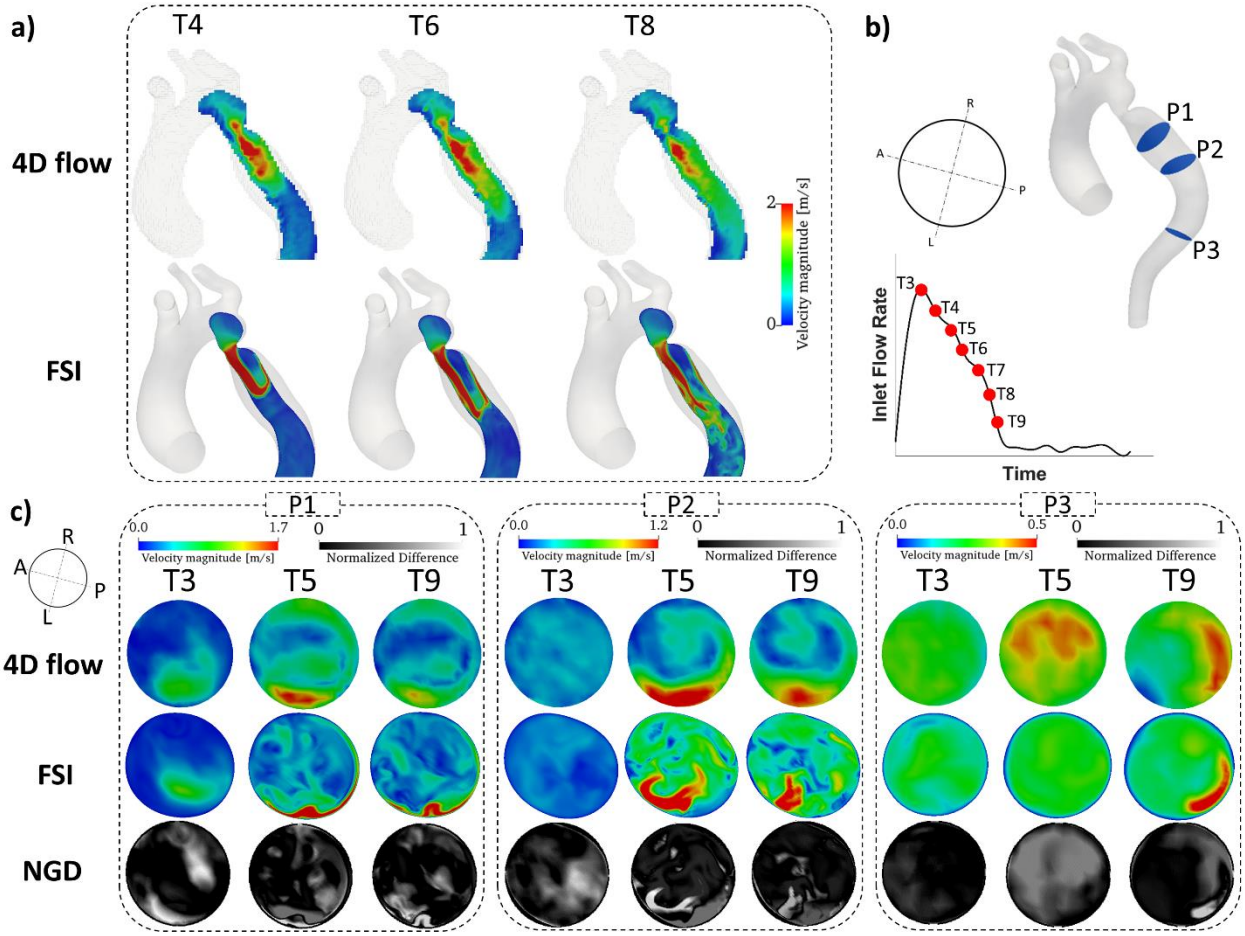

Figure 4. (a) Velocity magnitude contours on a sagittal plane in the descending aorta: comparison between 4D flow data and FSI results. (b) Representation of the 3D geometry used to analyze simulation results, cross-sectional planes are represented with their orientation together with time points in the cardiac cycle. (c) Velocity magnitude contours obtained from 4D flow data and FSI together with their normalized grayscale difference (NGD) images for the three cross-sections along the descending aorta.

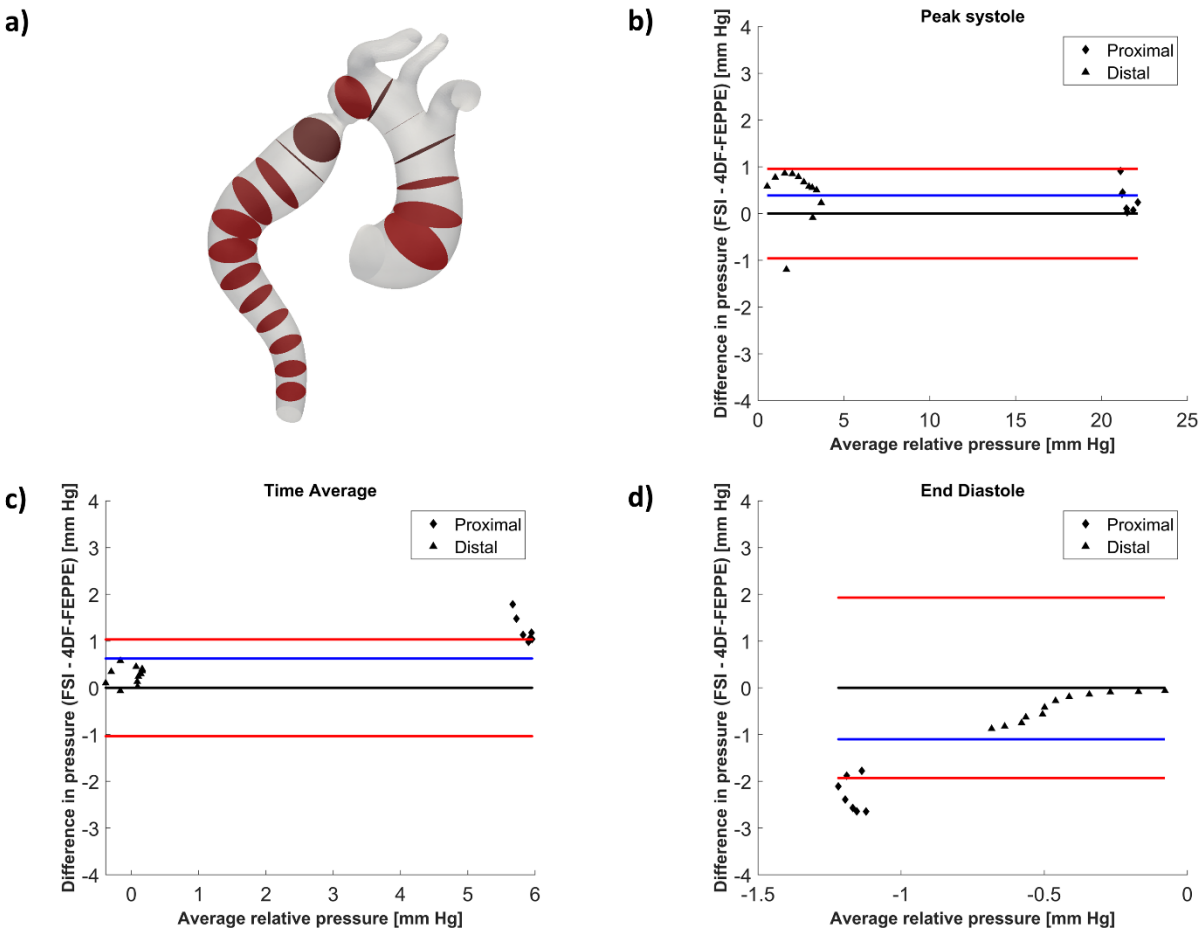

535

536 **Figure 5.** Pressure comparison: (a) cross-sections along the aorta where pressure was analysed. Bland-Altman plots

537 for (b) peak systolic, (c) time-averaged and (d) end-diastolic pressures differences obtained with FSI and 4DF-FEPPE

538 for the selected locations. Values corresponding to regions proximal and distal to the coarctation are represented

539 with diamonds and triangles respectively.

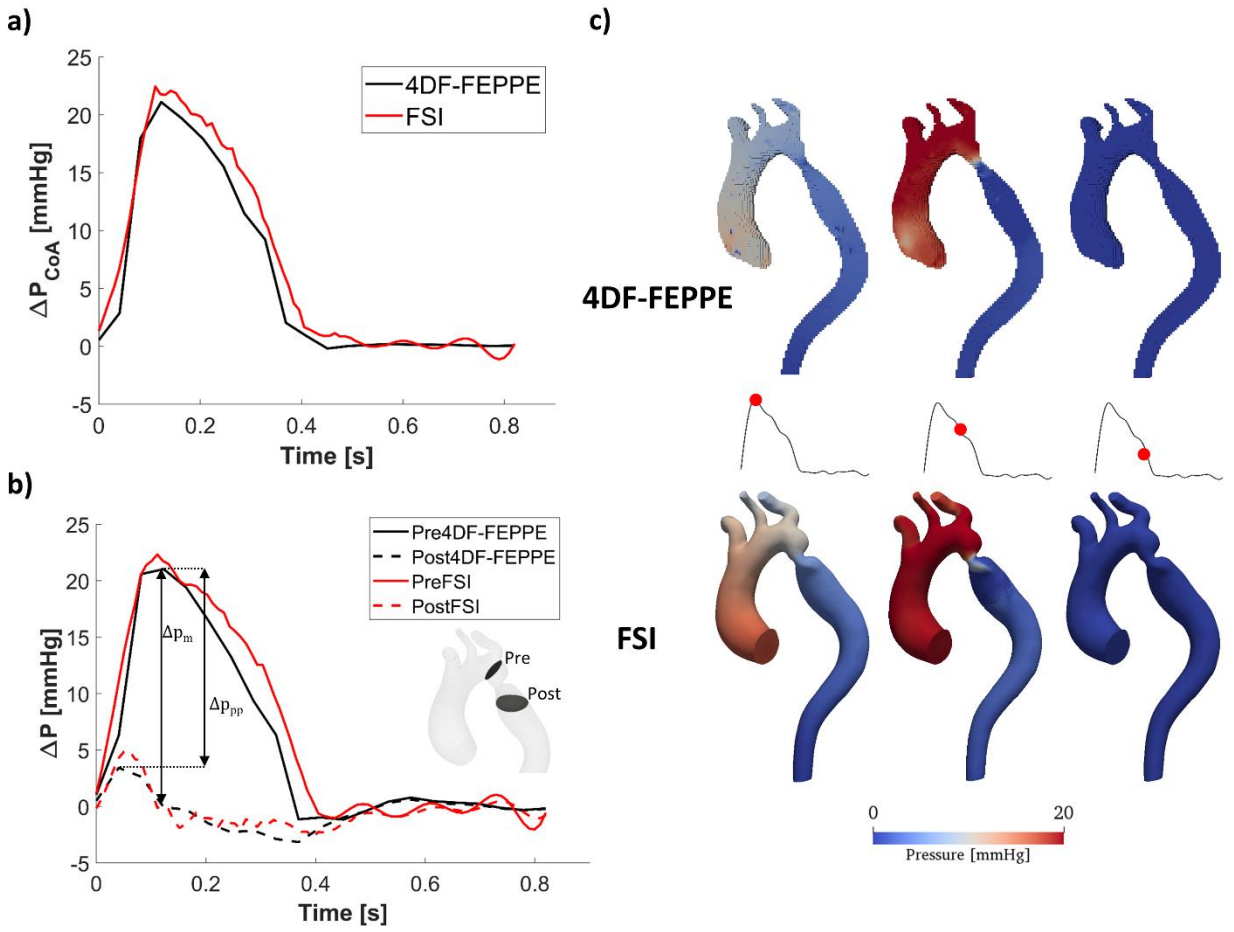

Figure 6. Trans-coarctation pressure drop comparison: (a) instantaneous trans-coarctation pressure drop: 4D flow-based curve calculated with 4DF-FEPPE (black line) vs. simulation results (red line). (b) Pressure differences between a section proximal (Pre) to the CoA and the DAo (continuous lines), together with pressure differences between a section distal (Post) to the CoA and the DAo (dashed lines) calculated from 4DF-FEPPE (black) and FSI results (red); cross-section-averaged values over time are shown. The different definitions for peak-to-peak (Δp_{pp}) and maximum (Δp_m) pressure drops are shown for the 4D flow-derived curves. (c) Pressure difference contours calculated with 4DF-FEPPE (top row) and with the FSI simulation (bottom row). Pressure differences are calculated with respect to the DAo.